Nature of surface-enhanced coherent Raman scattering

Xia Hua,[1,*] Dmitri V. Voronine,[1,2,†] Charles W. Ballmann,[1] Alexander M. Sinyukov,[1]
Alexei V. Sokolov,[1] and Marlan O. Scully[1,2,3]

[1]*Texas A&M University, College Station, Texas 77843-4242, USA*
[2]*Baylor University, Waco, Texas 76798, USA*
[3]*Princeton University, Princeton, New Jersey 08544, USA*

Surface-enhanced coherent nonlinear optical signals can dramatically improve detection sensitivity of spectroscopic imaging techniques. Large enhancement factors (EFs) of many orders of magnitude are expected for coherent Raman scattering of molecules in local fields of plasmonic nanostructures. However, only small EFs, several orders of magnitude less than the predicted values, were experimentally observed. To understand this discrepancy we measured the spatial variation of the shape of surface-enhanced coherent anti-Stokes Raman scattering (SECARS) spectra of pyridazine on randomly aggregated gold nanoparticles. We developed a model to simulate the dependence of SECARS spectra on the position and linewidth of the surface plasmon resonance, and attribute small (and even negative) EFs to local destructive interference. We report measurements of nanoscale phase effects in SECARS, and propose strategies to increase experimental EFs towards theoretical predictions.

PACS number(s): 42.65.Dr, 07.79.Fc

I. INTRODUCTION

Coherent nonlinear optical spectroscopy provides rich information about the structure and dynamics of atoms and molecules [1]. Various techniques such as second-harmonic generation (SHG), third-harmonic generation (THG), sum- and difference-frequency mixing, four-wave mixing (FWM), coherent Raman scattering, and others, in a wide range of frequencies from microwaves to x rays, probe rotational, vibrational, and electronic motion. Coherent Raman scattering microscopy, in particular, provides chemical maps of live cells and tissues, and has been used in biomedical applications [2–4]. Extension of these techniques to the nanoscale is challenging. Various strategies have been used to suppress the nonresonant background of coherent Raman signals based, for example, on polarization [5], phase effects [6–8], frequency modulation [9], time delay [10], and laser pulse shaping [11–15]. New nano-optical methods have been developed to enhance weak signals and to obtain nanoscale resolution [16]. Surface enhancement of linear optical signals due to strong local fields of plasmonic nanostructures has been successfully used in fluorescence, absorption, and spontaneous Raman scattering experiments [17–20]. However, surface-enhanced coherent nonlinear optical signals have been less explored. For example, proof-of-principle demonstrations of surface-enhanced SHG and THG [21–23], FWM [15,24–26], and coherent anti-Stokes Raman scattering (SECARS) [27–37] have been reported, but the expected large enhancement factors (EFs) were not observed.

Surface plasmon resonances (SPRs) of metallic nanostructures can lead to a strong local field enhancement. The amplitude, position, and linewidth of SPRs depend on the size and shape of nanostructures, and may be tuned by varying structural parameters. Nanostructures can have responses with complex amplitude and phase profiles due to several overlapping resonances. The realistic nanostructures can be synthesized by self-assembly or fabricated using nanolithography. Both methods have certain advantages and limitations, and produce nanostructures with imperfections that result in distributions of SPR properties. For example, randomly aggregated gold or silver nanoparticles can be self-assembled to form fractal-like clusters with a distribution of localized spatial regions of enhanced electric fields, called "hot spots" [38]. Near-field EFs in hot spots reach $\sim 10^1$–10^3. Molecules placed in such fields may generate optical signals enhanced by many orders of magnitude. Incoherent spontaneous Raman scattering signal intensity (I_{Raman}) is proportional to the number of molecules (N) and to the intensity of the incident field (I_{in}): $I_{\mathrm{Raman}} \sim N I_{\mathrm{in}}$. SPRs can enhance both the incident (E_{in}) and the scattered (E_{Raman}) fields by $\sim 10^1$–10^3, resulting in $\sim 10^4$–10^{12} enhancement factors $\mathrm{EF}_{\mathrm{Raman}} \sim |E_{\mathrm{in}}|^2 |E_{\mathrm{Raman}}|^2$. Such strong surface-enhanced Raman scattering (SERS) signals with EFs close to the theoretical values have been observed [17,18,20,39].

Coherent nonlinear optical signals have a higher order dependence on incident electric fields, and can, therefore, have larger enhancement factors than linear signals. For example, the intensity of coherent anti-Stokes Raman scattering (CARS) signals I_{CARS} is proportional to the squared number of molecules and to the intensities of three incident fields, pump (E_{pu}), Stokes (E_{St}), and probe (E_{pr}): $I_{\mathrm{CARS}} \sim N^2 |E_{\mathrm{pu}}|^2 |E_{\mathrm{St}}|^2 |E_{\mathrm{pr}}|^2$. Therefore, one can expect $\sim 10^8$–10^{24} enhancement factors from local fields of plasmonic nanostructures: $\mathrm{EF}_{\mathrm{CARS}} \sim |E_{\mathrm{pu}}|^2 |E_{\mathrm{St}}|^2 |E_{\mathrm{pr}}|^2 |E_{\mathrm{CARS}}|^2$ (compared to the conventional CARS). An additional chemical enhancement of $\sim 10^2$ has been predicted [40]. These surface-enhanced CARS (SECARS) signals could be used to extend nonlinear Raman microscopy to the nanoscale resulting in many applications. However, until now, several orders of magnitude smaller EFs than those expected for SECARS have been observed, and the reason for this remained unclear. Maximum enhancement of SECARS over conventional CARS signals of $\sim 10^{12}$ was predicted for silver nanospheres [28], but only $\sim 10^1$–10^3 was observed [29,30,35,41]. Other substrates were also explored

---

*Corresponding author: huaxia@tamu.edu
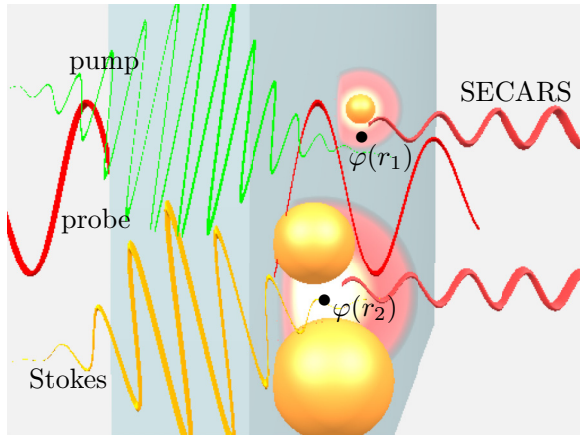†Secondary corresponding author: dmitri.voronine@gmail.com

FIG. 1. (Color online) Schematic picture of the surface-enhanced coherent Raman scattering process. Three ultrashort laser pulses are focused on the sample of randomly aggregated gold nanoparticles on the surface of glass inducing SECARS signals from pyridazine molecules in hot spots of the nanoparticles. Different hot spots have different local phases $\varphi(r)$ which lead to different shapes of the SECARS spectra. Averaging over several spots leads to destructive interference and decreases enhancement factors.
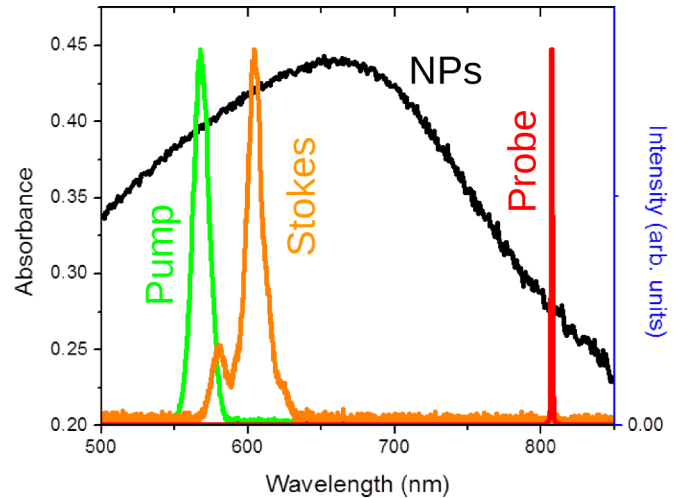

FIG. 2. (Color online) Absorbance spectrum of the aggregated gold nanoparticles (black, NPs) overlapping with the laser pulse spectra (pump, Stokes, and probe) used in the SECARS experiments.

such as randomly aggregated nanoparticles [33,37] and structured nanovoid substrates, including Klarite [36]. These substrates yielded EFs $\sim 10^5$–10^7, which were also smaller than expected, and the measured spectra had large nonresonant background contributions. The SECARS EFs over SERS are expected to be on the same order of magnitude as SERS EFs over spontaneous Raman signals. However, in [36] these were $\sim$4 orders of magnitude lower. These discrepancies between the predictions and observations may be resolved by considering the SPR properties such as the local phase and resonant enhancement of surface-enhanced coherent Raman signals.

Here we investigate these effects by measuring the spatial dependence of the shape of SECARS spectra of pyridazine molecules on the surface of randomly aggregated gold nanoparticles (Fig. 1). We also simulate the dependence of the shape of the SECARS spectra on the SPR position and line-width and use a simple model to explain the results of the measurements. We obtain insights into the nature of surface-enhanced coherent Raman scattering, which allow improving nanostructure design and experimental conditions. These improvements may lead to further signal enhancement resulting in applications in nanoscale bioimaging and ultra-sensitive detection.

II. EXPERIMENTAL RESULTS

SECARS experiments were performed using the experimental setup described earlier [37]. Briefly, femtosecond pump and Stokes (FWHM $\sim$ 60 fs) and picosecond probe (FWHM $\sim$ 1–2 ps) laser pulses were centered at 560, 600, and 805 nm, respectively (Fig. 2), and were generated using an amplified femtosecond Ti:sapphire laser system (Coherent, Inc.) with two optical parametric amplifiers with 1 kHz repetition rate. The probe pulse was shaped by a variable slit of a home-built

pulse shaper to have a top-hat-like spectrum. The probe pulse was thus stretched to a picosecond duration and acquired a temporal sinc shape. The pulses were collinearly focused using a 10 cm focal length lens onto the sample of liquid pyridazine sandwiched between two glass slides. Random gold nanoparticle (NP) aggregates were deposited onto the surface of the first glass slide along the laser beam propagation direction. The diameter of the individual gold NPs was 10–20 nm. They formed aggregates upon deposition on glass with surface roughness of 10–300 nm measured by atomic force microscopy (MultiView 4000, Nanonics Ltd.). This surface roughness is necessary for surface plasmon excitation to support a large range of frequencies. The randomly aggregated NPs formed a nonuniform thin film whose overall thickness can be controlled by varying the concentration of gold NPs in solution. Even though the roughness can be on the order of 300 nm, it strongly depends on the position on the sample. These surface irregularities result in hot spots with strong field confinement and enhancement and with a broad SPR frequency range (500–850 nm) revealed in the absorbance spectrum (Fig. 2). The center frequencies of the CARS excitation laser pulses were chosen to fit the SPRs.

The sample preparation procedure was previously described [37]. We used a modified procedure that was previously reported to produce randomly aggregated gold NPs on glass substrates [33,42]. The synthesis was performed by reduction of HAuCl$_4$ with sodium citrate [33,42,43]: 100 ml of 0.1 mM aqueous solution of HAuCl$_4$ was stirred and heated until boiling. Then 10 ml of 0.4 mM aqueous solution of trisodium citrate was added. As a result, individual spherical gold NPs 10–20 nm in diameter were obtained. Microscope slides were cleaned using concentrated sulfuric acid (98%) overnight, trichloroethylene (30 min), acetone (30 min), and methanol (30 min). All the steps were performed at room temperature. Distilled water was used to rinse the substrates. The glass slides were derivatized with 3-mercaptopropyltrimethoxysilane (MPTMS). Clean glass slides were kept in a 5% MPTMS solution in methanol for

24 h [42]. After derivatization, the slides were cleaned with methanol and rinsed with distilled water. Then the gold NPs were deposited onto the glass surface. After ∼2 h, a layer of aggregated gold NPs was formed.

The excitation laser focal spots of ∼10 μm diameter were centered on the thin layer of gold NP aggregates extending over a region including glass, gold, and pyridazine (Fig. 1). Resonantly excited gold NP aggregates generate many hot spots within the focal region [38], leading to various sources of CARS and nonresonant background. Glass, gold, and pyridazine generate the nonresonant FWM background. Glass occupies the largest volume within the focal spot and therefore we assume glass to be the primary source of the background. This background from glass can be suppressed by stronger focusing of the incident beams on the gold NPs. Then the background from the NPs will dominate [15,44]. CARS signals originate from bulk pyridazine or from pyridazine in the near field of the gold NPs. We assume that CARS signals originate mostly from the near field of the gold NPs due to the absence of the bulk signal without NPs [37]. We used 12-μm-thick pyridazine samples with gold NPs to perform these measurements. However, no signals were obtained in the absence of NPs under similar conditions. Additional evidence for these assumptions is provided by the results of the present experiments in the spatial dependence of the shape of CARS spectra. No spatial dependence of the CARS shape is expected for bulk samples. The phase of the background is determined by the three incident laser pulses interacting with glass, but the phase of the SECARS signal is determined by the local near fields induced by the gold NP aggregates. The relative phase difference between the background and the local fields determines the shape of the SECARS spectra.

The experimental results are shown in Fig. 3. SECARS spectra were measured with laser beams focused on different spots on the sample. All three laser pulses (pump, Stokes, and probe) were overlapped in time. Therefore, the nonresonant background was not suppressed. The power of the beams at the sample was 50, 50, and 100 μW for the pump, Stokes, and probe, respectively. No visible damage or loss of signal over the time period of several hours was observed. No CARS signal was obtained from bulk pyridazine between two glass slides without gold NPs. However, strong SECARS signals were observed in the presence of gold NPs. The positions of the pyridazine spectral lines (vertical lines in Fig. 3) agreed with previous measurements of the vibrational spectra [45,46]. The resulting SECARS spectra showed peaks [Fig. 3(a)], dips [Fig. 3(c)], and intermediate shapes [Fig. 3(b)] which depend on the spatial position of the focused laser beams on the sample. The intermediate shapes were more frequently observed. Different spectral shapes observed at different spots demonstrate the local phase effects of the gold NP aggregates, which have different phase profiles, $\varphi(r)$, as shown schematically in Fig. 1 due to different responses to the incident laser fields. Many nanosize hot spots with different local phases contribute to the averaged CARS signals collected from the illuminated ∼10 μm spot on the sample. These nano hot spots interfere and generate the total phase which varies from one spot to another. The measured SECARS spectral shape depends on the relative phase between the local fields and the background. If the background is absent (e.g., suppressed by pulse shaping), only the peaks are observed (not shown). However, the SECARS signals from different hot spots still interfere, decreasing the overall EF. Here, we use the background to reveal the presence of these interferences via the measurements of the spatial dependence of the shape of SECARS spectra. We estimated the measured EFs ∼4–6 × 10^7 using the following approach [37]. We estimate the EFs based on a direct comparison of the signals with and without NPs. CARS signal intensity can be expressed as [47]

$$I_{\text{CARS}} \sim I_{\text{pu}} I_{\text{St}} I_{\text{pr}} L^2 \text{sinc}^2 \left[\frac{\Delta k L}{2} \right]. \qquad (1)$$

For perfect phase matching, we estimate EF by comparing the SECARS signals obtained from a 12-μm-thick layer of pyridazine on randomly aggregated gold NPs (Signal$_{\text{NPs}}$) and a 2 mm cell of pure pyridazine without NPs (Signal$_{\text{no NPs}}$) for selected spectral peaks as

$$\text{EF} = \frac{\text{Signal}_{\text{NPs}} / L^2_{\text{NPs}}}{\text{Signal}_{\text{no NPs}} / L^2_{\text{no NPs}}}. \qquad (2)$$

III. SIMULATIONS

To better understand the spatial behavior of the SECARS spectra, we used a simplified model of gold NP aggregates by multiplying the pump, Stokes, and probe electric fields by Lorentzian response functions whose amplitudes and phases were scanned in the range of ∼550–950 nm. Gaussian laser pulse shapes $E_j(\omega) = \exp[-2\ln(2)(\frac{\omega-\omega_{jo}}{\Delta\omega_j})^2]$ were used to induce the CARS signals, where $j = 1,2$ stands for pump and Stokes, respectively, ω_{jo} is the center frequency of the jth pulse, and $\Delta\omega_j$ is the corresponding bandwidth. The picosecond probe pulse was modeled by $E_{\text{pr}}(\omega) = 1$ if
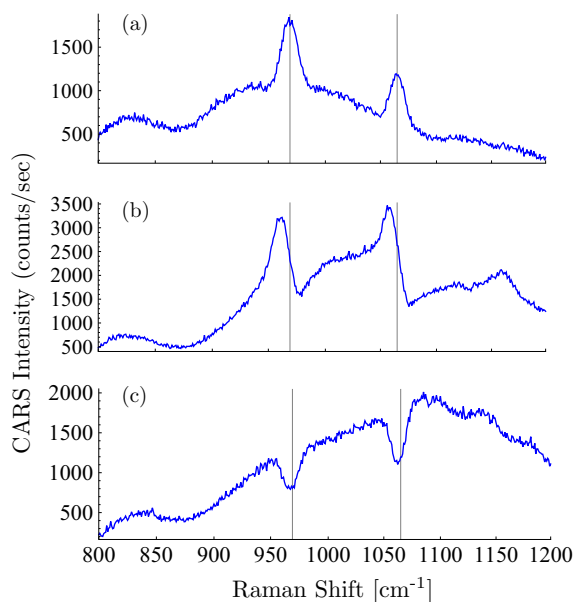

FIG. 3. (Color online) (a)–(c) Experimental SECARS spectra of pyridazine on random gold NP aggregates from different focal spots on the sample.
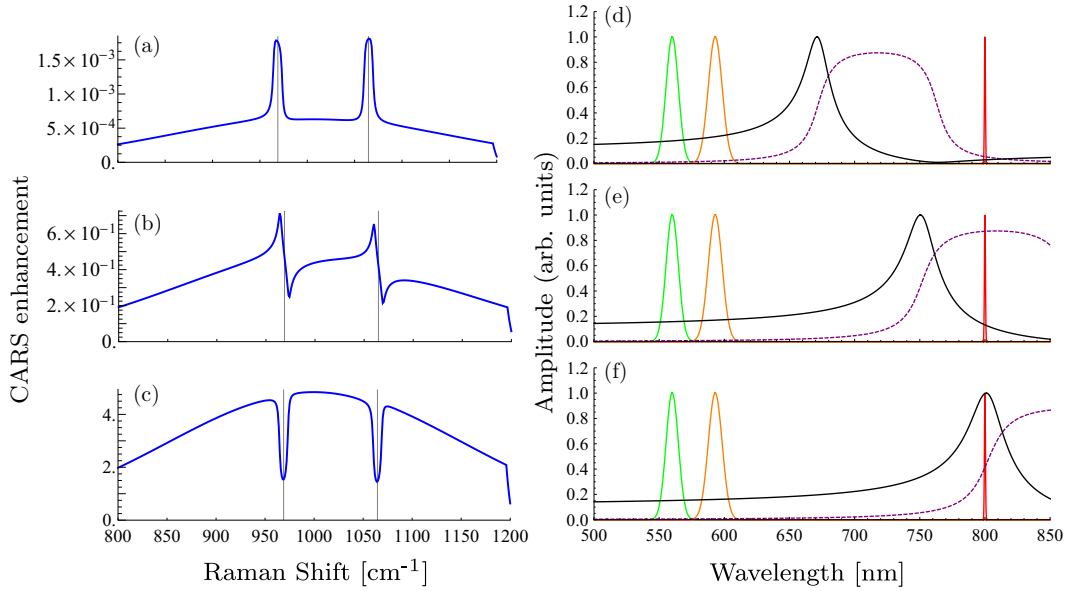
FIG. 4. (Color online) SECARS spectra of pyridazine simulated with a Lorentzian response with HWHM $\Delta \sim 200$ cm^{-1}, local field enhancement $A_{EF} = 10$ and SPR wavelength at (a) 672, (b) 751, and (c) 802 nm. The corresponding electric field spectral amplitudes of the incident pump (green), Stokes (orange), and probe (red) laser pulses with normalized amplitudes (solid black) and phases (purple dashed) of the local field enhancement $F(\omega)$ are shown in (d), (e), and (f), respectively.

$|\omega - \omega_{pr}|/\alpha \leqslant 5$ cm^{-1}, and 0 otherwise, where $\alpha = 2\pi c$ and c is the speed of light.

The nanoparticle response was modeled by a Lorentzian function [48], and the local field enhancement was given by

$$F(\omega') = 1 + \frac{A_{EF}\Delta}{\Omega_R - \omega' - i\Delta}, \tag{3}$$

where Ω_R is the SPR frequency, Δ is the half-width at half maximum (HWHM) of the Lorentzian, and A_{EF} is the local field enhancement factor. The unity term in Eq. (3) accounts for the incident electric field.

The third-order nonlinear polarization was modeled by [1]

$$P^{(3)}(\omega) = \int_0^\infty \left[\chi_{NR}^{(3)}(\Omega)S_{12,NR}(\Omega) + \chi_R^{(3)}(\Omega)F(\omega - \Omega)\right.$$
$$\left. \times S_{12,R}(\Omega)\right]E_3(\omega - \Omega)d\Omega, \tag{4}$$

where $\chi_R^{(3)}$, the resonant third-order nonlinear susceptibility, is given by

$$\chi_R^{(3)}(\omega') = \sum_k \frac{A_k\Gamma_k}{\Omega_{Rk} - \omega' - i\Gamma_k}, \tag{5}$$

$S_{12,NR}$ is

$$S_{12,NR}(\Omega) = \int_0^\infty E_1(\omega'')E_2^*(\omega'' - \Omega)d\omega'', \tag{6}$$

and $S_{12,R}$ is

$$S_{12,R}(\Omega) = \int_0^\infty F(\omega'')E_1(\omega'')F^*(\omega'' - \Omega)E_2^*(\omega'' - \Omega)d\omega''. \tag{7}$$

A_k is a constant related to the Raman cross section, Γ_k gives the Raman line halfwidth (~ 1 cm^{-1}) [49], Ω_{Rk} is the kth molecular vibrational resonance frequency, and the asterisk denotes complex conjugate. The SECARS signal intensity

is given by $I_{CARS}(\omega) \propto |P^{(3)}(\omega)|^2$. The simulations were performed in MATHEMATICA 8.

The simulation results are shown in Fig. 4. Two vibrational lines of pyridazine were chosen at ~ 968 and 1064 cm^{-1} based on the experimental values. The SECARS spectra were simulated using a Lorentzian response with $\Delta \sim 200$ cm^{-1}, $A_{EF} = 10$, and three values of the SPR wavelength at 672, 751, and 802 nm. The corresponding SECARS spectra are shown in Figs. 4(a), 4(b), and 4(c), respectively. The incident electric field spectral amplitudes and the response amplitudes and phases are shown for these three cases in Figs. 4(d), 4(e), and 4(f), respectively. The response phase (purple dashed) varies from 0 to π across the SPR and goes back to 0 at longer wavelengths due to the vanishing contribution of the Lorentzian response to the local field enhancement $F(\omega)$ as shown in Eq. (3). The total phase of the field is therefore equal to the phase of the incident field at longer wavelengths. During the scan of the SPR frequency, the phase of the SECARS signals also changed from 0 to π. This caused interference of the signals with the background and transformed SECARS peaks into dips (Fig. 4). The phase of the background was kept zero. This corresponds to the phase of the incident fields. Peaks, dips, and intermediate shapes of the SECARS spectra simulated using a simplified model in Figs. 4(a)–4(c) are in agreement with those obtained in the experiments on a more complicated system in Figs. 3(a)–3(c). The model gives insight into the mechanism of SECARS and allows describing the main spectral features using realistic parameters. For example, the chosen SPR and laser pulse frequencies coincide with the experimental values [37].

The model also gives insight into the signal enhancement. The CARS enhancement in Figs. 4(a)–4(c) was calculated by comparing CARS signals with and without the Lorentzian response, i.e., with $A_{EF} = 10$ and $A_{EF} = 0$, respectively. The

SECARS EFs are plotted on the y axes of Figs. 4(a)–4(c). Small and even negative EFs are obtained. This is due to the fact that the local field enhancement $F(\omega)$ in Eq. (3) is close to zero in a range of frequencies where the amplitude of the Lorentzian is approximately unity and the phase is π. In other words, the local field of the nanostructure can interfere destructively with the incident field and lead to suppression instead of enhancement of the CARS signals, generating "cold spots" instead of "hot spots." The dip in the $F(\omega)$ profile (solid black) is clearly seen in Fig. 4(d) around 750 nm in the vicinity of the CARS signal and the probe pulse. This leads to the smallest EF $\sim 10^{-3}$ shown in Fig. 4(a).

IV. DISCUSSION

The spatially resolved changes in SECARS interfering signals may be observed after averaging if one type of hot spots dominates in a particular excitation region. This is expected because the hot spots have different amplitudes and depending on the geometry some may be stronger than others. Two typical experimental SECARS spectra in Fig. 5(a) show peak (blue) and dip (red) patterns at different spots on the sample. These spectra are averages over a distribution of hot spots within the laser focus. Increasing the focal diameter leads to further averaging and decreases the EF. Figure 5(a) shows the results of averaging over ten spots (black). A dramatic signal suppression is observed. The simplified model reveals a similar behavior. Figure 5(b) shows two typical spectra with SPRs centered at 672 and 802 nm resulting in peaks (blue) and dips (red), respectively. Averaging over four spectra with SPRs at 672, 751, 802, and 892 nm results in a suppressed signal (black) in Fig. 5(b).

In the experiments, many hot spots are expected to contribute to the measured SECARS signals due to the high roughness of the surface and availability of a large number of closely spaced nanoparticles. The measured signals have the averaged phase which can reveal the averaged information on the statistical distribution of different kinds of hot spots within the excitation region. This distribution of different phases leads
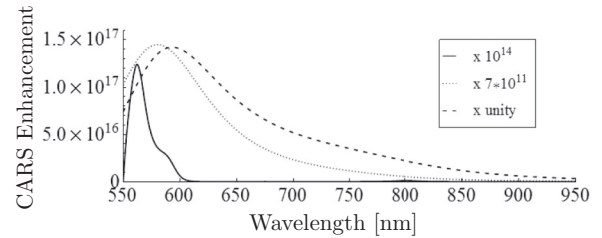
FIG. 6. Simulated CARS enhancement as a function of SPR frequency for different SPR linewidth and local field enhancement: (solid) $\Delta = 201.6$ cm^{-1}, $A_{\mathrm{EF}} = 10$; (dotted) $\Delta = 2016$ cm^{-1}, $A_{\mathrm{EF}} = 10$; (dashed) $\Delta = 2016$ cm^{-1}, $A_{\mathrm{EF}} = 1000$. Legend shows scale factors multiplied to the data to fit curves on graph.

to destructive interference and decreases the magnitude of the CARS signals. We consider this phase effect as the primary source of the discrepancy between the predicted large and the observed small EFs. This problem may be addressed by laser pulse shaping. Here we used unshaped incident Gaussian laser pulses. Adaptive [50,51] and deterministic [52,53] near-field control methods may be used to compensate these phase effects and minimize destructive interference.

Another effect which contributes to the CARS enhancement is the spatial mode overlap of the local electric fields enhanced by plasmonic nanostructures. We investigate this effect by simulating SECARS signals as a function of the SPR frequency and linewidth. Figure 6 shows the simulated CARS enhancement of the 968 cm^{-1} line of pyridazine for different SPR parameters: (solid) $\Delta = 201.6$ cm^{-1}, $A_{\mathrm{EF}} = 10$; (dotted) $\Delta = 2016$ cm^{-1}, $A_{\mathrm{EF}} = 10$; (dashed) $\Delta = 2016$ cm^{-1}, $A_{\mathrm{EF}} = 1000$. These plots show optimal SPR frequencies to achieve the maximum CARS enhancement for the specific arrangement of laser pulse configurations used in the experiments. The distribution of SPR frequencies in random gold NP aggregates further reduces the CARS EFs and should be taken into account when designing the substrates and laser pulse configurations. The SPR linewidth $\Delta = 2016$ cm^{-1} corresponds to single NPs [54] and the reduced $\Delta = 201.6$ cm^{-1} to NP aggregates. SPRs of complex nanostructures can be described as Lorentzian oscillators with the number of Lorentzians, near-field EFs, and linewidths varying depending on the nanostructure geometry. The broad SPR spectrum in Fig. 2 is an average over many hot spots with different linewidths. Each particular hot spot has a narrower linewidth than the average. Therefore, the observed EFs may be further reduced due to the challenge of matching the three CARS pulse center frequencies to the plasmonic resonances.

The gold film is not uniform with an average thickness of 500–800 nm measured by AFM, and is better described as a collection of diffusion-limited fractal-like aggregates with various SPRs. Larger values of A_{EF} also correspond to NP aggregates and to specially designed plasmonic substrates. Figure 6 shows that for $A_{\mathrm{EF}} = 1000$ and $\Delta = 2016$ cm^{-1}, the CARS enhancement of EF $\sim 10^{17}$ may be obtained. To achieve such EFs in experiments, one has to take into account the local phase effects described above. One approach is to use high quality periodic substrates with a narrow distribution of SPR linewidths and frequencies [36]. As an example, we considered a periodic
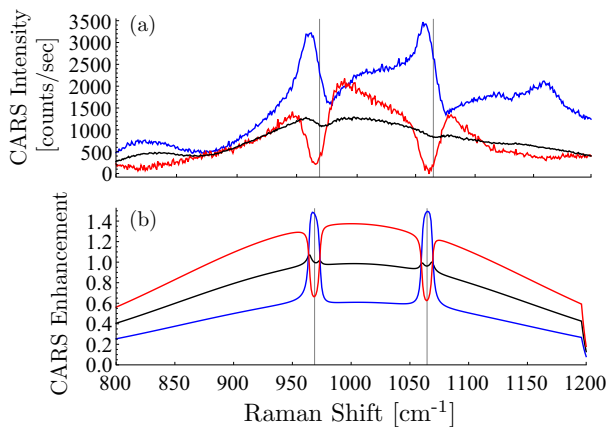

FIG. 5. (Color online) Experimental (a) and simulated (b) SE-CARS spectra of pyridazine: peaks (blue), dips (red), and averaged (black) spectra. Ten spots were averaged in (a) and four spots were averaged in (b). In both cases, averaging decreased the SECARS signal magnitude.

array of cross-dipole nanoantennas made of gold strips of 43 nm length, 10 nm width, and 10 nm height with $\sim$128 near-field enhancement above the dipole gap in the plane 15 nm above the surface [55]. The corresponding SECARS EFs of $\sim$$10^{11}$ and $\sim$$10^{12}$ were calculated for these nanostructures with typical SPR linewidths of 140 and 230 meV, respectively.

V. CONCLUSION

In summary, we provide insights into the nature of surface-enhanced coherent nonlinear optical signal enhancement and investigate the dependence of surface-enhanced coherent Raman scattering on SPR parameters. We measured the spatial dependence of the SECARS spectra of pyridazine on random gold NP aggregates and used a simplified model to understand the experimental results. Similar effects may be present in SERS experiments. However, SERS is an incoherent technique and there is no FWM background that can reveal the local phases. We attribute the previously measured small SECARS EFs to destructive interference and SPR distribution effects,

and report the first measurements of nanoscale phase effects in SECARS using the interference of the CARS signals and FWM background. This approach provides information about the local phase of the nanostructures and may be extended to the subwavelength scale. We propose strategies to improve the signal enhancement by many orders of magnitude. Our results may be used to extend other related techniques such as FAST CARS [56] to the nanoscale.

[1] S. Mukamel, *Principles of Nonlinear Optical Spectroscopy* (Oxford University Press, New York, 1999).

[2] A. Zumbusch, G. R. Holtom, and X. S. Xie, Phys. Rev. Lett. **82**, 4142 (1999).

[3] J.-X. Cheng and X. S. Xie, *Coherent Raman Scattering Microscopy* (CRC Press, Boca Raton, FL, 2013).

[4] C.-Y. Chung, J. Boik, and E. O. Potma, Annu. Rev. Phys. Chem. **64**, 77 (2013).

[5] J. Cheng, L. Book, and X. Xie, Opt. Lett. **26**, 1341 (2001).

[6] E. Potma, C. Evans, and X. Xie, Opt. Lett. **31**, 241 (2006).

[7] M. Jurna, J. P. Korterik, C. Otto, J. L. Herek, and H. L. Offerhaus, Phys. Rev. Lett. **103**, 043905 (2009).

[8] X. Wang, A. Zhang, M. Zhi, A. V. Sokolov, G. R. Welch, and M. O. Scully, Opt. Lett. **35**, 721 (2010).

[9] F. Ganikhanov, C. Evans, B. Saar, and X. Xie, Opt. Lett. **31**, 1872 (2006).

[10] A. Volkmer, L. Book, and X. Xie, Appl. Phys. Lett. **80**, 1505 (2002).

[11] D. Pestov *et al.*, Science **316**, 265 (2007).

[12] A. C. W. van Rhijn, M. Jurna, A. Jafarpour, J. L. Herek, and H. L. Offerhaus, J. Raman Spectrosc. **42**, 1859 (2011).

[13] G. Volpe, S. Cherukulappurath, R. J. Parramon, G. Molina-Terriza, and R. Quidant, Nano Lett. **9**, 3608 (2009).

[14] D. Brinks, R. Hildner, F. D. Stefani, and N. F. van Hulst, Opt. Express **19**, 26486 (2011).

[15] Y. Wang, C. Y. Lin, A. Nikolaenko, V. Raghunathan, and E. O. Potma, Adv. Opt. Photon. **3**, 1 (2011).

[16] L. Novotny and B. Hecht, *Principles of Nano-Optics* (Cambridge University Press, New York, 2006).

[17] K. Kneipp, M. Moskovits, and H. Kneipp, *Surface-Enhanced Raman Scattering: Physics and Applications* (Springer, New York, 2006).

[18] E. C. L. Ru and P. G. Etchegoin, *Principles of Surface-Enhanced Raman Spectroscopy and Related Plasmonic Effects* (Elsevier, Amsterdam, 2008).

[19] C. D. Geddes, *Metal-Enhanced Fluorescence* (Wiley, New York, 2010).

[20] S. Schluecker and W. Kiefer, *Surface Enhanced Raman Spectroscopy* (Wiley, New York, 2011).

[21] R. Antoine, P. F. Brevet, H. H. Girault, D. Bethell, and D. Schriffin, Chem. Commun. **19**, 1901 (1997).

[22] A. Bouhelier, M. Beversluis, A. Hartschuh, and L. Novotny, Phys. Rev. Lett. **90**, 013903 (2003).

[23] M. Lippitz, M. A. van Dijk, and M. Orrit, Nano Lett. **5**, 799 (2005).

[24] D. S. Chemla, J. P. Heritage, P. F. Liao, and E. D. Isaacs, Phys. Rev. B **27**, 4553 (1983).

[25] P. Genevet, J.-P. Tetienne, E. Gatzogiannis, R. Blanchard, M. A. Kats, M. O. Scully, and F. Capasso, Nano Lett. **10**, 4880 (2010).

[26] E. Poutrina, C. Ciracì, D. J. Gauthier, and D. R. Smith, Opt. Express **20**, 11005 (2012).

[27] C. K. Chen, A. R. B. de Castro, Y. R. Shen, and F. DeMartini, Phys. Rev. Lett. **43**, 946 (1979).

[28] H. Chew, D.-S. Wang, and M. Kerker, J. Opt. Soc. Am. B **1**, 56 (1984).

[29] E. J. Liang, A. Weippert, J. M. Funk, A. Materny, and W. Kiefer, Chem. Phys. Lett. **227**, 115 (1994).

[30] N. Hayazawa, T. Ichimura, M. Hashimoto, Y. Inouye, and S. Kawata, J. Appl. Phys. **95**, 2676 (2004).

[31] T. Ichimura, N. Hayazawa, M. Hashimoto, Y. Inouye, and S. Kawata, Phys. Rev. Lett. **92**, 220801 (2004).

[32] T. W. Koo, S. Chan, and A. A. Berlin, Opt. Lett. **30**, 1024 (2005).

[33] C. J. Addison, S. O. Konorov, A. G. Brolo, M. W. Blades, and R. F. B. Turner, J. Phys. Chem. C **113**, 3586 (2009).

[34] S. Schlücker, M. Salehi, G. Bergner, M. Schütz, P. Ströbel, A. Marx, I. Petersen, B. Dietzek, and J. Popp, Anal. Chem. **83**, 7081 (2011).

[35] V. Namboodiri, M. Namboodiri, G. I. Cava Diaz, M. Oppermann, G. Flachenecker, and A. Materny, Vib. Spectrosc. **56**, 9 (2011).

[36] C. Steuwe, C. F. Kaminski, J. J. Baumberg, and S. Mahajan, Nano Lett. **11**, 5339 (2011).

[37] D. V. Voronine, A. M. Sinyukov, X. Hua, K. Wang, P. K. Jha, E. Munusamy, S. E. Wheeler, G. Welch, A. V. Sokolov, and M. O. Scully, Sci. Rep. **2**, 891 (2012).

[38] V. M. Shalaev, *Nonlinear Optics of Random Media* (Springer, New York, 1999).

[39] E. C. Le Ru, E. Blackie, M. Meyer, and P. G. Etchegoin, J. Phys. Chem. C **111**, 13794 (2007).

[40] J. A. Parkhill, D. Rappoport, and A. Aspuru-Guzik, J. Phys. Chem. Lett. **2**, 1849 (2011).

[41] T. Ichimura, N. Hayazawa, M. Hashimoto, Y. Inouye, and S. Kawata, J. Raman Spectrosc. **34**, 651 (2003).

[42] C. J. Addison and A. G. Brolo, Langmuir **22**, 8696 (2006).

[43] J. R. Anema, A. G. Brolo, A. Felten, and C. Bittencourt, J. Raman Spectrosc. **41**, 745 (2010).

[44] H. Kim, C. Xiang, A. G. Guell, R. M. Penner, and E. O. Potma, J. Phys. Chem. C **112**, 12721 (2008).

[45] H. D. Stidham and J. V. Tucci, Spectrochim. Acta Part A **23**, 2233 (1967).

[46] Y. Ozono, Y. Nibu, H. Shimada, and R. Shimada, Bull. Chem. Soc. Jpn. **59**, 2997 (1986).

[47] D. S. Choi, S. C. Jeoung, and B. H. Chon, Opt. Express **16**, 2604 (2008).

[48] C. F. Bohren and D. R. Huffman, *Absorption and Scattering of Light by Small Particles* (Wiley, New York, 2007).

[49] J. Vázquez, J. J. L. Gozález, F. Márquez, and J. E. Boggs, J. Raman Spectrosc. **29**, 547 (1998).

[50] M. Aeschlimann, M. Bauer, D. Bayer, T. Brixner, F. J. García de Abajo, W. Pfeiffer, M. Rohmer, C. Spindler, and F. Steeb, Nature (London) **446**, 301 (2007).

[51] M. Aeschlimann, T. Brixner, S. Cunovic, A. Fischer, P. Melchior, W. Pfeiffer, M. Rohmer, C. Schneider, C. Strüber, P. Tuchscherer, and D. V. Voronine, IEEE J. Sel. Top. Quantum Electron. **18**, 275 (2012).

[52] P. Tuchscherer, C. Rewitz, D. V. Voronine, F. J. García de Abajo, W. Pfeiffer, and T. Brixner, Opt. Express **17**, 14235 (2009).

[53] M. Aeschlimann, M. Bauer, D. Bayer, T. Brixner, S. Cunovic, A. Fischer, P. Melchior, W. Pfeiffer, M. Rohmer, C. Schneider, C. Strüber, P. Tuchscherer, and D. V. Voronine, New J. Phys. **14**, 033030 (2012).

[54] C. Sönnichsen, T. Franzl, T. Wilk, G. von Plessen, J. Feldmann, O. Wilson, and P. Mulvaney, Phys. Rev. Lett. **88**, 077402 (2002).

[55] R. Nevels, G. R. Welch, P. S. Cremer, P. Hemmer, T. Phillips, S. Scully, A. V. Sokolov, A. A. Svidzinsky, H. Xia, A. Zheltikov, and M. O. Scully, Mol. Phys. **110**, 1993 (2012).

[56] M. O. Scully, G. W. Kattawar, R. P. Lucht, T. Opatrný, H. Pilloff, A. Rebane, A. V. Sokolov, and M. S. Zubairy, Proc. Natl. Acad. Sci. USA **99**, 10994 (2002).